ADVANCED FUNCTIONAL MATERIALS
www.afm-journal.de

Modelling Thermal Halide Exchange of Perovskite Powders With and Without $BMIMBF_4$ From an Interdiffusion Perspective

Tobias Siegert, Prerna Pahwa, Markus Griesbach, Frank-Julian Kahle, Harald Oberhofer, Anna Köhler, and Helen Grüninger**

Halide migration limits the stability of hybrid halide perovskites for optoelectronic applications, yet can be decelerated at room temperature by adding ionic liquids. An approach is presented to quantitatively evaluate the diffusion of I^- and Br^- to form $MAPbI_xBr_{3-x}$ from neat perovskite powders. First, in situ X-ray diffraction (XRD) data are used to extract the time-dependent $MAPbI_xBr_{3-x}$ composition of an initially physical mixture of neat $MAPbI_3$ and $MAPbBr_3$ grains. Next, an effective interdiffusion model is expanded to obtain time-dependent diffusion coefficients. They reduce with time due to the decreasing concentration gradient during the halide exchange process. In samples without any additive, Br^- is found to diffuse up to three times faster into the $MAPbI_3$ grains than I^- into the $MAPbBr_3$ grains, while the addition of the ionic liquid 1-Butyl-3-methylimidazolium tetrafluoroborate ($BMIMBF_4$) accelerates and nearly equalizes the interdiffusion. Analyzing the temperature dependence of the diffusion coefficient suggests that, without ionic liquid, the diffusivities are limited by the halide vacancy formation. In contrast, in the presence of the ionic liquid, halide vacancy formation is facilitated, yet is controlled by the thermal activation of the $BMIM^+$ mobility.

1. Introduction

Lead halide perovskites have recently become silicon's leading contender in solar cell materials.[1] This material class possesses an ABX_3 lattice structure, where the monovalent A-site cation is usually Cs^+, methylammonium (MA^+), or formamidinium (FA^+), the divalent B-site cation consists of Pb^{2+} or Sn^{2+}, and the X-site anion is I^-, Br^-, or Cl^-.[2] As the bandgap can easily be tuned via stoichiometric variations in A, B, or X sites, perovskites are a promising candidate for multi-junction solar cells.[3–6]

The bandgap of halide perovskites can be tuned continuously by varying the halide composition. For example, substituting I^- with Br^- in MA-based perovskites allows changing the band gap from 1.3 up to 2.2 eV for Sn-based perovskites and from 1.6 up to 2.2 eV for Pb-based perovskites.[7–10] However, halide segregation, i.e., the reversible demixing of halide ions to form, for example, I^-- or Br^--rich domains,[11] limits the commercialisation of perovskite-based devices.[12] Many studies have analysed the influence of external and internal factors on halide segregation. External stimuli include humidity,[13] light intensity,[14] oxygen concentration,[15] pressure,[16] temperature,[17] electric fields,[18] and charge carrier transport layers between the perovskite and electrodes.[19] Internal factors comprise the character of the A-site cations,[20] grain size,[21] strain,[22] and defects.[23] Several models based on different aspects have been proposed to explain the phenomenon of

T. Siegert, M. Griesbach, F.-J. Kahle, A. Köhler
Soft Matter Optoelectronics
University of Bayreuth
95447 Bayreuth, Germany
E-mail: anna.koehler@uni-bayreuth.de

P. Pahwa, H. Oberhofer
Theoretical Physics VII – Computational Materials Design
University of Bayreuth
95447 Bayreuth, Germany

P. Pahwa, H. Oberhofer, H. Grüninger
Bavarian Center for Battery Technology (BayBatt)
University of Bayreuth
95447 Bayreuth, Germany
E-mail: helen.grueninger@uni-bayreuth.de

A. Köhler
Bayreuth Institute of Macromolecular Research (BIMF) and Bavarian Polymer Institute (BPI)
University of Bayreuth
95447 Bayreuth, Germany

H. Grüninger
Inorganic Chemistry
University of Bayreuth
95447 Bayreuth, Germany

The ORCID identification number(s) for the author(s) of this article can be found under https://doi.org/10.1002/adfm.202510920

DOI: 10.1002/adfm.202510920

halide segregation in hybrid perovskites.[24–26] Despite all this research, a complete understanding of the process has yet to be achieved, and the missing pieces to bring the models together have yet to be found. In any case, however, the underlying problem is connected to ion migration in the bulk and across interfaces.

A common approach to reducing ion migration is the use of additives.[27] Among these, one additive class often used is a range of ionic liquids (ILs) consisting of cations and anions.[28] A widely used subclass is based on cations with an imidazolium core and halogen or superhalogen anions, e.g. 1-Butyl-3-methylimidazolium tetrafluoroborate ($BMIMBF_4$).[29,30] The IL imidazolium cations, which can exhibit a wide variety of sidechains, are too large for incorporation in the perovskite lattice.[29,31,32] Hence, they are located at surfaces and grain boundaries where they may form a passivation layer. A similar ionic radius for BF_4^- and I^- indicates that the superhalogen can saturate iodide vacancies.[33–36] In any case, however, it is agreed that both, cation and anion can passivate surface defects. The ionic liquid $BMIMBF_4$ is known to increase film quality and device performance of halide perovskites.[31]

We recently studied the impact of adding $BMIMBF_4$ to $MAPbI_3$ and $MAPbBr_3$ powders with the aim to better understand its role in the halide exchange process. At room temperature, the addition of $BMIMBF_4$ decelerates the migration of I^- and Br^- in the powders, as intended.[37] However, when the powders are heated to 55–90 °C, we find that the addition of $BMIMBF_4$ increases the thermal halide exchange.[38] In this earlier study, we used X-ray diffraction (XRD), photoluminescence, and nuclear magnetic resonance (NMR) spectroscopy on $MAPbI_3$ and $MAPbBr_3$ powders with and without $BMIMBF_4$ to obtain a qualitative model of how the IL accelerates halide exchange at elevated temperatures while it passivates the grain surface at room temperature.

Here, we use our previous XRD data to develop a refined, quantitative understanding of the halide exchange process in the presence and absence of $BMIMBF_4$. The XRD data are particularly suitable as they allow for a quantitative analysis of the global phase composition as a function of time. For the analysis, we build on a well-established average effective interdiffusion coefficient concept.[39] Average effective interdiffusion coefficients are usually calculated to describe the alloying of different metals.[39–44] Recently, the interdiffusion of O^{2-} and F^- in barium ferrate perovskite-type systems was described in the framework of an average effective interdiffusion process.[45] We apply this approach to the thermally activated halide exchange between $MAPbI_3$ and $MAPbBr_3$ powders, which results in the formation of the solid solution $MAPbI_{1.5}Br_{1.5}$. We expand it to extract time and temperature dependant interdiffusion coefficients for both halides, I^- and Br^-. In the absence of an IL, the bottleneck to the interdiffusion process is identified to be a kinetically hindered I^- diffusion into $MAPbBr_3$ grains, most likely due to higher barriers for Br^- vacancy formation. This is no longer the case in the presence of $BMIMBF_4$, as the $BMIM^+$ cation seems to assist in removing Br^- from lattice sites at the grain boundary surface, thus facilitating Br^- vacancy formation and hence iodide penetration at the $MAPbBr_3$ interface. The rate limiting process is then the thermal activation of $BMIM^+$ mobility.

2. Methods

The XRD experiment is described in full in Ref. [38], and data acquisition details are repeated here in the Supporting Information section A. In brief, two mechanochemically synthesized perovskite powders, $MAPbI_3$ and $MAPbBr_3$, in the following called parent perovskites, were physically mixed in a cryo-ball mill under liquid nitrogen temperatures. The resulting physical mixture was then heated to three different temperatures, 60, 75, and 90 °C, and held at that temperature to induce the halide exchange process. The time period for heating the sample to the temperature was ≈15 min. After reaching the terminal temperature, the evolution of the perovskite crystal lattice from the mixture of neat compositions to the multicomponent solid solution $MAPbI_xBr_{3-x}$ was monitored in situ by XRD. A scheme of the experiment and the obtained XRD data is displayed in **Figure 1**.[38] For each XRD pattern, we used a data acquisition time of 3.5 min. The full XRD pattern from 10 to 50 °2θ before and after heating are available in Figure S1, (Supporting Information) and confirms the absence of any impurity or degradation phases. This experiment was then repeated for perovskite powders to which the ionic liquid $BMIMBF_4$ was added during their syntheses. In order to extract the phase composition, the XRD pattern at every time step was decomposed into 13 Gaussians of equal width at fixed 2θ positions, nominally representing $MAPbI_3$, $MAPbI_{2.75}Br_{0.25}$, ..., $MAPbI_{0.25}Br_{2.75}$, $MAPbBr_3$ compositions. These compositions resemble the multiple $MAPbI_{3-x}Br_x$ phases forming due to the thermally induced halide exchange.[38] The area of each Gaussian peak relative to the sum of all peaks corresponds to the fraction of the associated phase observed in the sample.

3. Results and Discussion

Figure 1b and c show the temporal evolution of the XRD pattern during mixing as heatmaps, exemplary for powders without and with the IL, held at 90 °C. The associated line cuts, shown in Figure 1d,e, display the XRD intensity versus 2θ, for three exemplary times, 0, 10, and 62 h. The corresponding Gaussian lines for each composition are coloured in shades from black to orange, respectively (c.f. Figure S2, Supporting Information). The overall evolution of the phase fractions for neat $MAPbI_3$, neat $MAPbBr_3$, and the sum of all mixed compositions are displayed in Figure 1f and g (c.f. Figure S3, Supporting Information for evolution over the full measurement time). The data for the temperatures 75 and 60 °C are available in Figures S4,S5 (Supporting Information).

For the perovskite powders without IL, at all temperatures studied, the neat $MAPbI_3$ phase decays faster than the neat $MAPbBr_3$ phase. In contrast, when powders with IL are used, the neat phases decay faster than without IL, and, moreover, at an approximately equal rate.[38] This implies that the transport of I^- and Br^- during the formation of the solid perovskite solutions is accelerated when the IL additive is present. We previously interpreted this to indicate an active role of the IL in the halide exchange process.[38] We suggested that, at low temperatures, the IL binds to the perovskite grain surfaces and saturates surface defects, thus passivating the defect sites. However, at elevated temperatures, the $BMIM^+$ cation becomes highly dynamic and no longer binds to the defect, thus rendering the defect site accessible. In addition, when leaving the defect site, it can take the

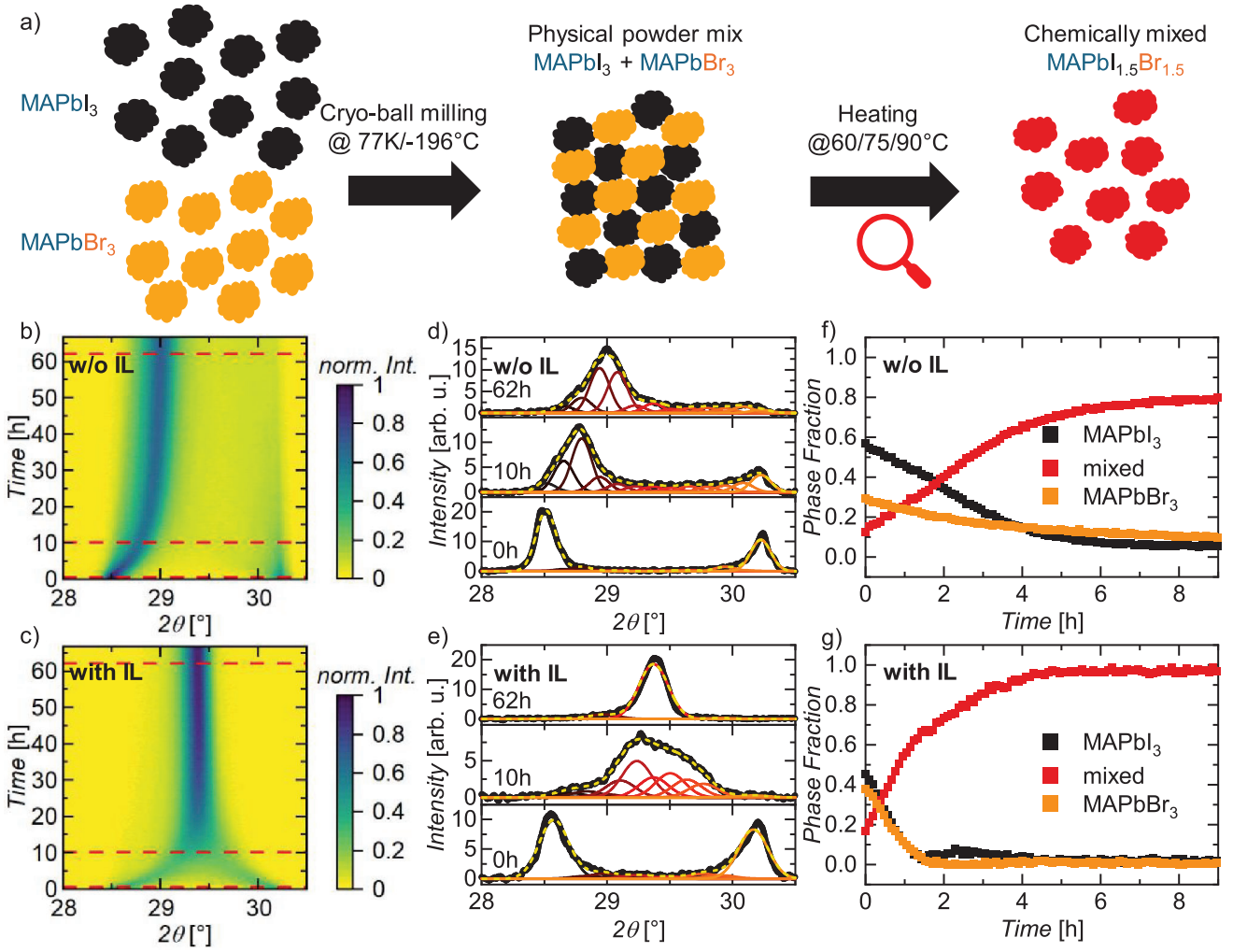

Figure 1. a) Schematic representation of the halide exchange experiment conducted in Ref. [38]. b, c) Temporal evolution of the XRD pattern of the perovskite powder mixtures at 90 °C without and with $BMIMBF_4$ (IL), respectively. d, e) XRD patterns (black dots) for powders without and with IL at 90 °C after selected times, fitted to a sum (dotted yellow line) of 13 Gaussian (redish lines) representing a gradually varying composition of $MAPbI_{3-x•0.25}Br_{0+x•0.25}$, x = 0, 1, ...12. f,g) Evolution of the phase fractions of $MAPbI_3$ (black), $MAPbBr_3$ (orange), and the sum of all mixed $MAPbI_{3-x•0.25}Br_{0+x•0.25}$ phases (red) for the powders without and with IL, respectively, at 90 °C.

halide anion there along. Our conclusion was that in particular, Br^- anions are transported by the IL cation $BMIM^+$.[46] Hence, the combined effect of opening the defect sites and transporting halides accelerates the ion diffusion in a way that results in equal diffusion for both halide species.

The driving force for the interdiffusion is the entropy gain when the concentration gradient between the grains reduces. Hence, I^- diffuse into the $MAPbBr_3$ grain and Br^- into the $MAPbI_3$ grain. XRD only monitors a resulting net halide diffusion between different perovskite compositions, i.e., halide migration within the same composition, known to happen in perovskites[47,48] is not detectable via XRD. The XRD patterns for the three different heating times of 0, 10, and 62 h at 90 °C with IL from Figure 1e is magnified in **Figure 2b**, along with the decomposition of the XRD peaks to 13 distinct halide compositions. These compositions and their respective halide concentrations can be translated into a concentration profile (Figure 2c) using a 1D model as follows.[39,45] We use the average pseudoradius of perovskite agglomerates, i.e., grains of the same perovskite type that stick together to form a larger particle. The pseudoradius is the radius of a circle with the same area as the cross-section of a halide perovskite agglomerate shown in the SEM images in Figure S7 (Supporting Information). We find the pseudoradius to be ≈0.7 µm for neat $MAPbI_3$ and $MAPbBr_3$, with and without IL. In the presence of interdiffusion, we expect a monotonous concentration gradient falling or rising from the interface. Obviously, the halide exchange happens at the interface. Thus, the fully mixed composition will eventually form there, with a compositional gradient toward the neat phases, $MAPbI_3$ and $MAPbBr_3$, which are furthest away from the interface. As the diffusion into a grain occurs from either side, it suffices to consider the concentration profile from the center of one grain to the center of the adjacent grain.

As mentioned, the 13 Gaussian peaks in the XRD pattern correspond to 13 distinct compositions, i.e., $MAPbI_3$, $MAPbI_{2.75}Br_{0.25}$, ..., $MAPbI_{0.25}Br_{2.75}$, $MAPbBr_3$. The intensity of

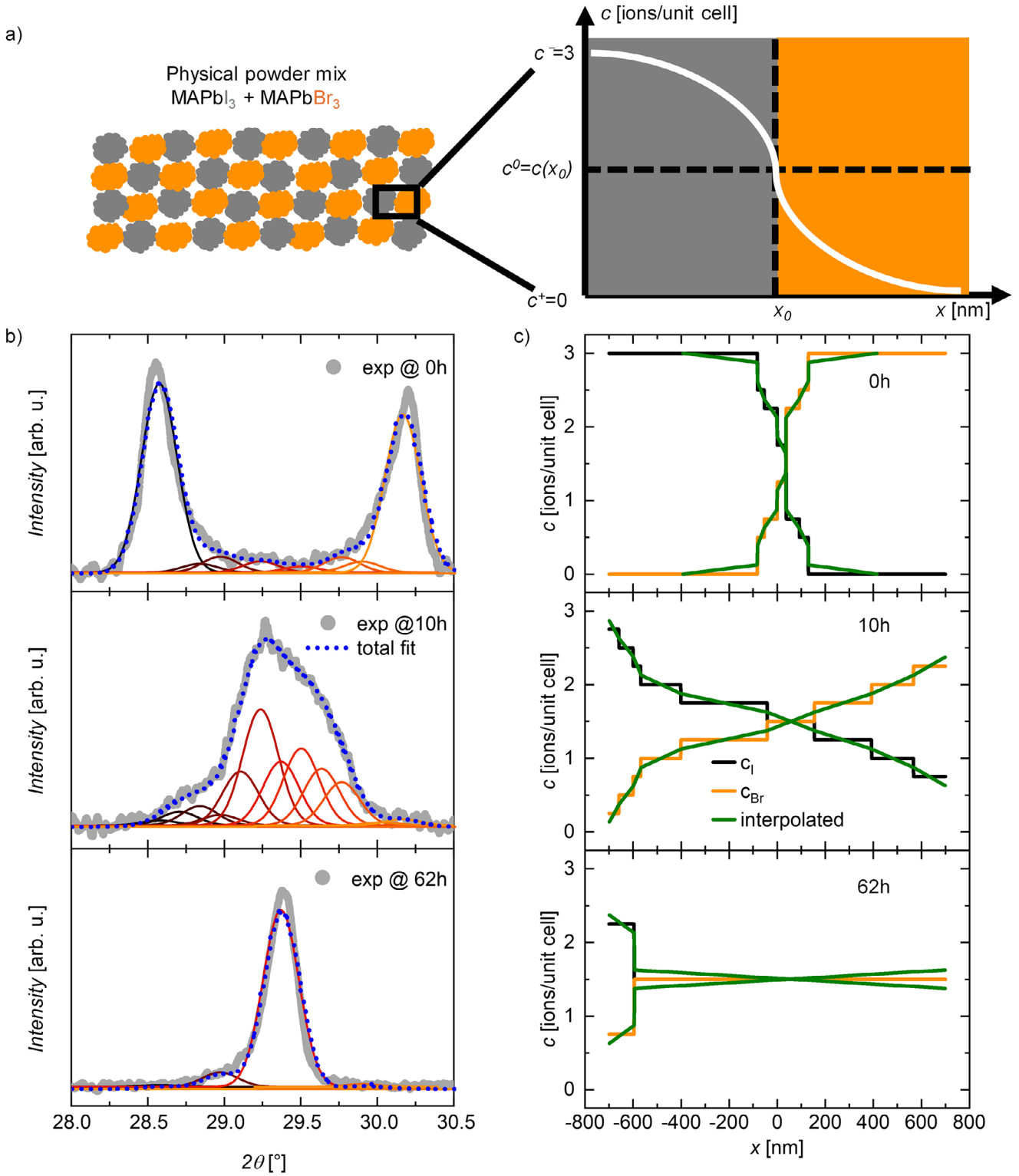

Figure 2. a) Scheme illustrating how the interface in a physical powder mixture is approximated as two adjacent 1D slabs of initially $MAPbI_3$ and $MAPbBr_3$. b) XRD patterns of the measurement with IL at 90 °C for three times 0, 10, and 62 h. The data (grey dots) are fitted (blue dashed line) to a sum of 13 Gaussian peaks (black to red solid lines) representing a gradually varying composition with discrete phases of $MAPbI_{3-x•0.25}Br_{0+x•0.25}$, x = 0, 1, ...12. c) I^- and Br^- concentration profiles derived from the 13 Gaussians, along with an interpolated profile.

each XRD peak correlates directly with the width of the associated compositional layer, corrected by a factor of 1.07 to account for the smaller lattice constant in $MAPbBr_3$ compared to $MAPbI_3$ (c.f. Supporting Information section E).[49–53] We can thus obtain a concentration profile for every time step from the XRD data.

As an example, Figure 2c displays the corresponding concentration profiles of I^- and Br^- for interdiffusion between perovskite powders with IL after 0, 10, and 62 h at 90 °C. At the start of the measurement, (0 h), we find an intermixed area of ≈100 nm to either side of the interface. We attribute this to beginning ion diffusion during the 15 min heating ramp prior to reaching the final temperature. After 10 h, mixed compositions ranging from $MAPbI_2Br_1$ to $MAPbI_1Br_2$, have spread up to ≈600 nm of either side of the interface. After 62 h, the composition is fully intermixed to a $MAPbI_{1.5}Br_{1.5}$ composition on the former neat $MAPbBr_3$ phase, while a 100 nm narrow a $MAPbI_{2.25}Br_{0.75}$ composition remains near the centre of the former neat $MAPbI_3$ grain.

For the further calculation of the average effective interdiffusion coefficients, we interpolate these concentration profiles linearly (green line in Figure 2c). This avoids artefacts in the further calculation resulting from discrete values (Supporting Information section F). The corresponding data without IL and data obtained at different temperatures are displayed in Supporting Information section G. Furthermore, Supporting Information section H shows the evolution of the concentration profiles for each measurement over time.

To obtain the average effective interdiffusion coefficient for I^- and Br^-, we follow the approach originally suggested by Dayananda,[39] related to the Boltzmann–Matano method.[54,55] This analysis has already been applied to describe the interdiffusion of O^{2-} and F^- in barium ferrate perovskite-type systems.[45] Dayananda considers the diffusion fluxes in a binary system, and based on the Onsager formalism and Fick's law, he derives the average effective interdiffusion coefficient for the left and right-hand side from the interface at every time step t according to[39]

$$\tilde{D}_R(t) = \frac{\int_{c^+}^{c^0} (x - x_0)^2 dc}{2t(c^0 - c^+)} \quad (1)$$

$$\tilde{D}_L(t) = \frac{\int_{c^0}^{c^-} (x - x_0)^2 dc}{2t(c^- - c^0)} \quad (2)$$

with c^+ and c^- denoting the concentration of the diffusing ion, e.g. iodine, at the right and left boundary, respectively, and c^0 being the value at the interface (c.f. Figure 2a). In our case, $\tilde{D}_R$ describes the diffusion of the iodide toward the right of the interface, i.e., into the Br-rich phases, and $\tilde{D}_L$ that of bromide toward the left into the I-rich phases. Note that this average effective diffusion coefficient is not an explicit function of time, but rather it is a constant value representing the time-integrated diffusion process up to the measured time t. Thus, the average effective diffusion coefficient changes as the concentration gradient changes with time.

For our discretized treatment, the integral in Equations (1) and (2) needs to be expressed as a sum. Using $x_0 = 0$, $c^0 = c_0$ and $c^+ = 0$, $c^- = 3$ and following reference,[39] we obtain the average effective interdiffusion coefficient $\tilde{D}_{eff,I}$ for I^- and $\tilde{D}_{eff,Br}$ for Br^- according to

$$\tilde{D}_{eff,I}(t) = \frac{\sum_j x_j^2 \Delta c_j}{2tc_0} \quad (3)$$

$$\tilde{D}_{eff,Br}(t) = \frac{\sum_j x_j^2 \Delta c_j}{2t(c^- - c_0)} \quad (4)$$

Here, x_j is the distance of the point j to $x = 0$ and Δc_j is the difference in the concentration of two adjacent concentration values. Applying Equations (3) and (4) to the data in Figure 2 results in the average effective interdiffusion coefficient displayed in **Figure 3a**. For the analysis of the mixing process, it is useful to consider the squared penetration depths. x_p^2 of both halides given by reference:[39]

$$x_p^2(t) = 2\tilde{D}_{eff}(t) \cdot t \quad (5)$$

$\sqrt{x_p^2(t)}$ indicates how far the ions penetrated up to the time t, and it is displayed in Figure 3b for samples held at 90 °C. x_p^2 for all temperatures and $\sqrt{x_p^2(t)}$ for samples at 75 °C and at 60 °C are available in Figures S20–S22 (Supporting Information). $\tilde{D}_{eff}$ gives the effective diffusivity, i.e., averaged over time from $t = 0$ to t. Thus, $2\tilde{D}_{eff}$ corresponds to the secant in the x_p^2 versus t plot (blue lines in **Figure 4**). We can derive the instantaneous diffusion coefficient at a particular time t, $D(t)$, by taking the tangent to $x_p^2(t)$ (Figure 3c, red lines in Figure 4).

$$D(t) = \frac{1}{2}\frac{dx_p^2}{dt} \quad (6)$$

The apparent time dependence of the diffusivity is a result of the change in concentration with time. $D(t)$ shows a decay over time that can be fitted well with a single exponential function. A closer look at the decay suggests that there is a decaying oscillation superimposed on the exponential decay. The intensity of this transient oscillation varies between different temperatures. Its origin is not entirely clear, but it might reflect the interdependence of I^- and Br^- interdiffusion, as well as morphological variations.

The average effective interdiffusion coefficients are generally higher than the time-dependent diffusion coefficients. We attribute this to the fact that we start with an already slightly intermixed interface at $t = 0$. The diffusion coefficients we obtain are in the range of 10^{-13} to 10^{-15} $cm^2\ s^{-1}$, similar to values reported in earlier work on single crystals in solutions,[54] a coupled mixed halide nanowire,[55] thin films pressed on each other,[56,57] and nanocrystals on nanowires.[58]

Comparing the samples for I^- and Br^- without IL, we find the average effective diffusion coefficient as well as the instantaneous diffusion coefficient for Br^- to be up to three times that of I^- (Figure S23, Supporting Information). This is also reflected in the larger diffusion length of Br^-. Figure 3 hence demonstrates that, in samples without IL, Br^- ions diffuse further and faster in the iodide-rich phase than I^- ions in the bromide-rich phase.

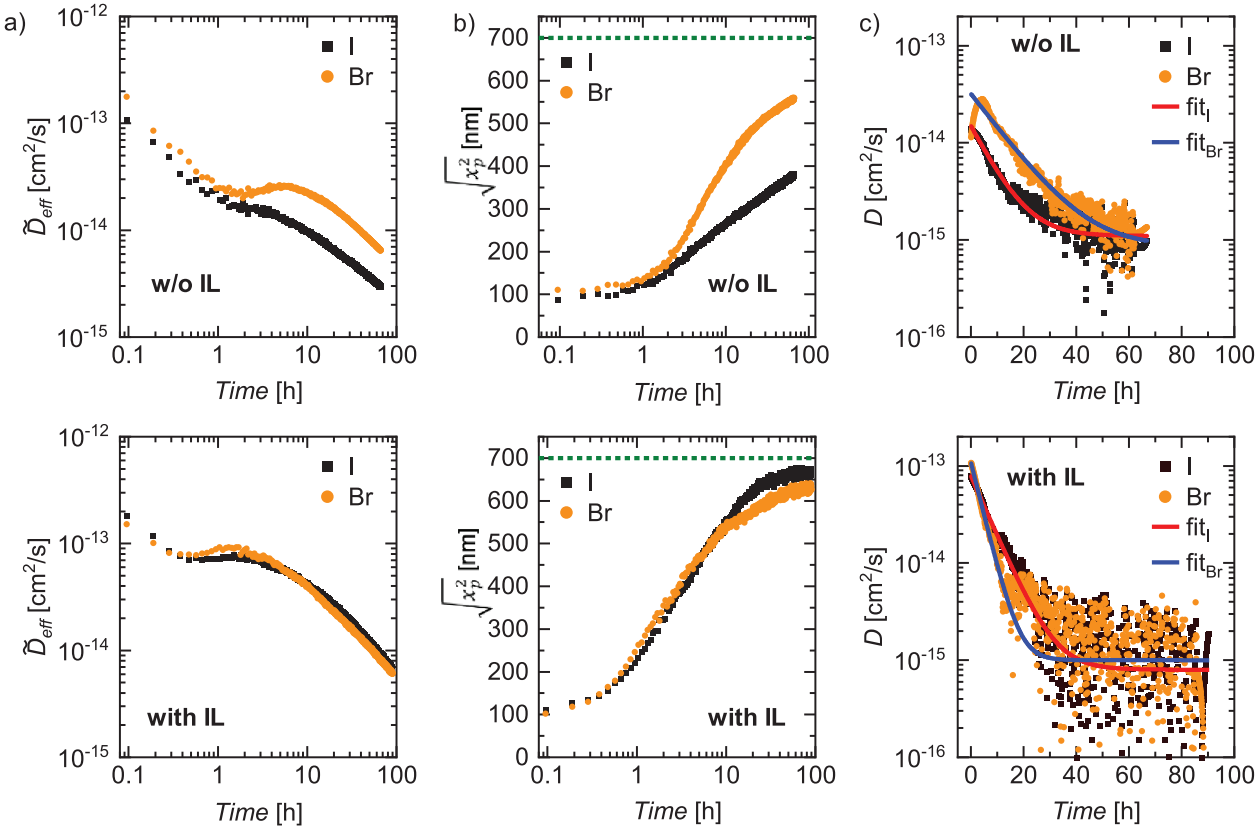

Figure 3. a) Average effective interdiffusion coefficient $\tilde{D}_{eff}$ at 90 °C without (top) and with (bottom) IL. b) The root mean square penetration depth obtained without (top) and with (bottom) IL. Green dotted lines represent the maximum diffusion length for the two ion species due to the finite grain size. c) The time-dependent diffusion coefficient D(t) without (top) and with (bottom) IL. Also shown are single exponential fits.

This is similar for temperatures of 75 and 60 °C (Supporting Information section J).

Our finding of a faster diffusion of Br^- in I-rich phases than of I^- in Br-rich phases in the absence of any IL is consistent with the existing body of work. It was also reported for studies of halide exchange between solution and single crystals,[54] and in thin films pressed on each other.[57] Previous studies attributed the lower diffusivity of I^- in $MAPbBr_3$ to higher barriers for Br^- vacancy formation,[59] and migration,[60–64] and concomitantly a lower defect density in $MAPbBr_3$.[60,65] This seems plausible, since i) the bond strength is higher for Pb—Br compared to Pb—I,[66] and ii) the smaller ionic radius of Br^- compared to I^- (196 pm vs 220 pm)[67] leading to a smaller lattice constant in $MAPbBr_3$ compared to $MAPbI_3$ (5.9 Å vs 6.3 Å).[49–53] This is confirmed by density functional theory (DFT) calculations on the Pb—Br and Pb—I bond strength in $MAPbI_3$ and $MAPbBr_3$, and the excess energy of halide interdiffusion as detailed in the Supporting Information section K. In brief, the energy contribution to the bond strength is found to be -0.82 and -0.75 eV for Pb—Br and Pb—I, using the Integrated Crystal Orbital Hamilton Population method.[68] This shows that the Pb—Br bond is ≈8% stronger than the Pb—I bond, also reflected in the Pb—Br bond distances of 3.02 Å versus Pb—I bond distance of 3.22 Å, supporting that Br^- vacancy formation has a higher barrier. Further, we calculated the excess energies[69,70] of $MAPbI_{3-x}Br_x$ and $MAPbBr_{3-x}I_x$ resulting from replacing an I^- (Br^-) ion in $MAPbI_3$ ($MAPbBr_3$) with a Br^- (I^-) ion. Here, we found a value of -0.77 eV for $MAPbI_{3-x}Br_x$ (x = 1/27), demonstrating that interdiffusion of Br^- into $MAPbI_3$ is energetically favourable. Contrary, we found a value of ~+5 meV for $MAPbBr_{3-x}I_x$ (x = 1/27), highlighting that interdiffusion of I^-

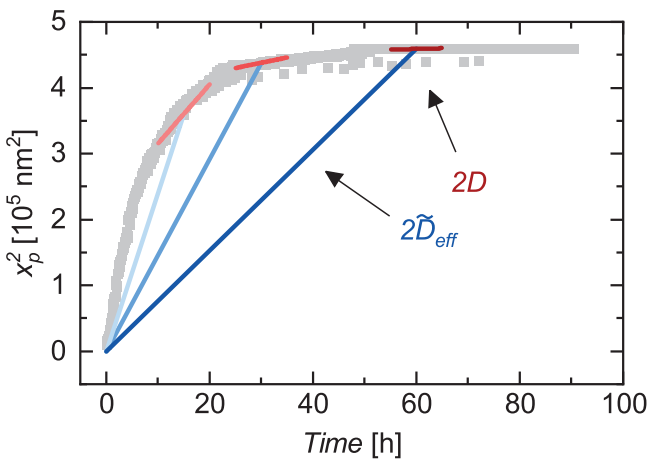

Figure 4. The difference between the average effective interdiffusion coefficient $\tilde{D}_{eff}$ (blue secants) and the time-dependent diffusion coefficient D (red tangents) exemplary on the squared penetration depth x_p^2 of I^- for the measurement at 90 °C with IL.

into $MAPbBr_3$ is impeded. Comparing the geometry-optimized structures of $MAPbI_{3-x}Br_x$ and $MAPbBr_{3-x}I_x$ further reveals that the softer $MAPbI_3$ lattice is able to deform in order to accommodate Br^- easily, while the stiff $MAPbBr_3$ lattice shows negligible deformation limiting I^- interdiffusion (Figure S25, Supporting Information). In summary, Br^- diffusion in $MAPbI_3$ via large I^- vacancies should be facile, while I^- diffusion in $MAPbBr_3$ may be impeded by the lack of Br^- vacancies and the smaller and stiffer $MAPbBr_3$ lattice.

When IL was added to the perovskite powders during syntheses, diffusion is accelerated for both, I^- and Br^-. In particular, both halide species show approximately the same diffusivity and diffusion length. This also applies to the samples held at 75 and 60 °C (Supporting Information section J), though the diffusion process slows down as the temperature reduces. This change upon IL addition shall be analyzed and discussed in detail further below.

The faster bromide diffusion in perovskite powders without IL may, at first sight, seem at odds with the faster decay of the neat $MAPbI_3$ phase shown in Figure 1. In our previous study, we interpreted the faster $MAPbI_3$ phase decay in pristine samples to indicate a faster iodide migration compared to bromide migration.[38] The accelerated $MAPbBr_3$ decay in the presence of the IL (Figure 1g) was interpreted as a pronounced acceleration of Br^- diffusion with IL. The data in Figure 3 show that IL accelerates the diffusion of both halides, with I^- being accelerated more than Br^-. The reason for this puzzle with regard to our previous conclusion is that previously, the focus was set solely on the decay of parent perovskite phases, i.e., the decay of $MAPbI_3$ and $MAPbBr_3$. In contrast, now we focus on the halide interdiffusion to form mixed halide phases. Consequently, the analyzed directions of diffusion are reversed, and we need to adjust our previous interpretation. A faster $MAPbI_3$ decay observed in pristine samples is caused by a fast diffusion of bromide into $MAPbI_3$ and thus reflects a higher Br^- diffusion coefficient. This reconciles the observation of Figure 1 and Figure 3.

In contrast to the conclusions from the XRD analysis, the results of the previously reported ^1H and ^{19}F MAS NMR measurements on the IL additive in the perovskites do not change with the direction of the analyzed diffusion process. While the mobility of the BF_4^- does not change at temperatures between 60 and 90 °C, $BMIM^+$ exhibits an increase in mobility.[38] Hence, the differences between the different temperatures can be attributed to the IL cation. Furthermore, the IL ions separate because of the tendency of $BMIM^+$ to bind to Br^-,[46] and the accumulation of BF_4^- on the surfaces of $MAPbI_3$ grains.[38] Nonetheless, no indications of the influences of the IL on the bulk perovskite could be found.[38] We note that ^1H and ^{19}F MAS NMR measurements published in our previous report give no hints for any thermal degradation of the $BMIMBF_4$ additive in our temperature range up to 90 °C.[38] Others reported degradation of the IL well above 300 °C.[71]

To further investigate the influence of the IL, we compare the measurements at different temperatures. We focus on mono-exponential fits to the time-dependent diffusion coefficients:

$$D(t) = D_0 \exp(-kt) + D_\infty \quad (7)$$

Table 1. Activation energies and pre-exponential factors for both halides at 90 °C with and without IL extracted from the Arrhenius plots in Figure 5.

	ion	without IL	with IL
E_A	I^-	31 kJ mol^{-1} (0.32 eV)	85 kJ mol^{-1} (0.88 eV)
	Br^-	57 kJ mol^{-1} (0.59 eV)	80 kJ mol^{-1} (0.83 eV)
D_0	I^-	$1.4 \cdot 10^{-14}$ cm^2 s^{-1}	$7.9 \cdot 10^{-14}$ cm^2 s^{-1}
	Br^-	$3.1 \cdot 10^{-14}$ cm^2 s^{-1}	$10.8 \cdot 10^{-14}$ cm^2 s^{-1}

A table listing all fit parameters (D_0, k and D_∞) for all temperatures studied is given in Table S1 (Supporting Information). The values for the diffusion coefficient extrapolated to the beginning of diffusion at $t = 0$, D_0, are summarized in **Table 1**, exemplary for the halide exchange at 90 °C with and without IL. The diffusivity of Br^- always exceeds that of I^-, yet when IL addition accelerates the initial diffusivity, the relative difference between both halides reduces.

To analyse the temperature dependence, the relevant quantity is the time-independent rate constant k that characterises the diffusion. k is a measure for how fast the concentration gradient that drives the interdiffusion disappears. An Arrhenius plot of the rate constant k on a semilogarithmic scale versus the inverse temperature yields the activation energy E_A from the slope of the linear regression (**Figure 5**).

The activation energies we find (31 to 85 kJ mol^{-1}) are comparable to those found in other halide exchange studies, with values ranging between 27 to 74 kJ mol^{-1} (0.28 to 0.77 eV) reported in references.[55,56,58,72,73] Furthermore, the activation energy for the remixing of segregated $MAPbI_xBr_{3-x}$ thin films is with 53.5 kJ mol^{-1} (0.55 eV), similar to our values.[14] The errors associated with the data in Table 1 are estimated to be ≈10 % of the values. This reflects the estimated systematic error, which exceeds the statistical error from fitting by at least one order of magnitude.

First, we discuss the activation energies for pristine samples and, subsequently, the impact of the IL. Without IL, the activation energy for the diffusion of Br^- in $MAPbI_3$ is significantly higher than for I^- diffusion in $MAPbBr_3$, as evident from the steeper slope in Figure 5c. We attribute this to higher barriers for Br^- vacancy formation resulting from the stronger Pb-Br bonds as discussed above. The vacancy formation, leading to free anions, may be the dominating factor determining the activation energy of the Br^- diffusion process. Once the barrier to free Br^-, i.e., the Br^- vacancy formation, is overcome, Br^- can diffuse easily in $MAPbI_3$ and in iodide-rich phases because of their larger lattice constants and the availability of iodide vacancies. Eventually, this leads to high decay rates.

We complement our previous interpretation[38] on the role of $BMIMBF_4$ in the thermally induced halide exchange process. We suggest that at room temperature, the additive cation $BMIM^+$ saturates undercoordinated iodide and bromide at perovskite grain interfaces. The interaction between $BMIM^+$ and the halide (X) in turn slightly weakens the X-Pb bonds of the respective halides to the perovskite lattice. We suggest that at elevated temperatures, these bonds may be broken up in favour of the halides binding to $BMIM^+$ and thus facilitating halide

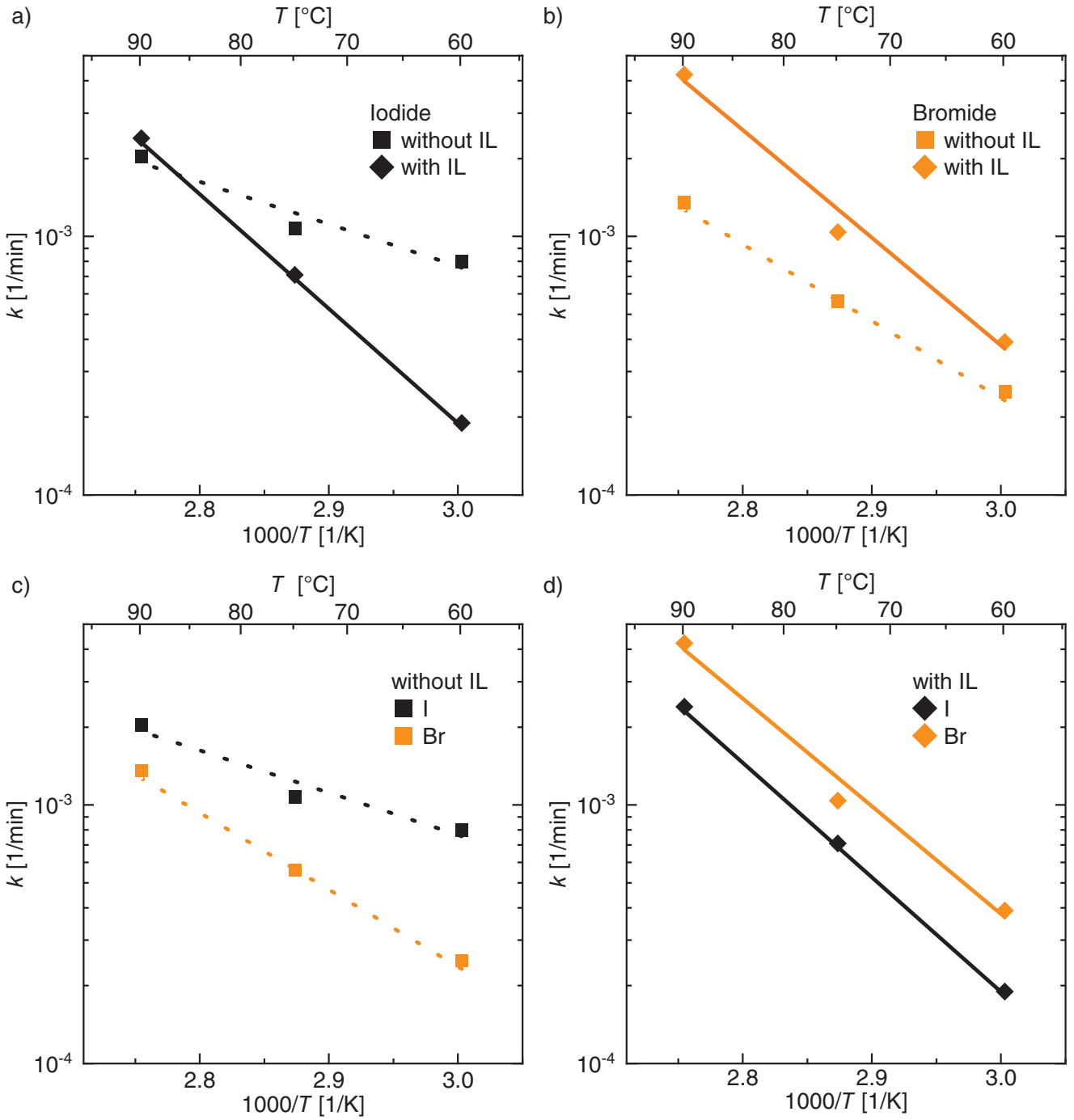

Figure 5. Arrhenius plots of the decay rate k of the time-dependent diffusion coefficient for a) I^- and b) Br^- with and without IL. c) and d) show the comparison between I^- and Br^- without and with IL.

vacancy formation, which results in an overall increase in diffusion coefficients (Figure 3, Table 1). However, as $BMIM^+$ binding to Br^- is preferred compared to I^-,[46] this effect will be more pronounced for bromide and thus facilitate particularly Br^- vacancy formation, which was the bottleneck for I^- diffusion into Br-rich phases. Additionally, the resulting $BMIM^+$-X^- complex may act as a vehicle and shuttle halides between grain interfaces. Again, due to the favoured interaction between $BMIM^+$ and Br^-, we expect a more facile release of iodide from the complex. This would result in a faster I^- exchange to grain interfaces and thus further reflect the stronger increase in I^- diffusion coefficients with IL (Figure 3, Table 1). In summary, the vacancy formation as well as the transport of halides is facilitated by the $BMIM^+$. The mobility of $BMIM^+$, however, is itself strongly temperature activated. Thus, the activation energy for the diffusion process in the presence of IL mainly reflects the activation energy for the $BMIM^+$

mobility and is therefore the same for both halides, i.e., ≈0.8–0.9 eV.

To evaluate the application of our approach on other systems, we have also analyzed previously measured halide interdiffusion with the ionic liquid $BMIMPF_6$ (Figure S26, Supporting Information).[38] The ionic radius of PF_6^- (254 pm) is bigger than BF_4^- (229 pm),[74] so that the interdiffusion may differ. However, we find that the effect of $BMIMPF_6$ on halide interdiffusion is similar to the influence of $BMIMBF_4$. This is, the diffusion process gets accelerated and the diffusion coefficient for I^- and Br^- become equal. We attribute this to the $BMIM^+$ cation as discussed above.

4. Conclusion

We present an approach to quantitatively evaluate halide diffusion in halide exchange processes in perovskites. We based our analysis on an average interdiffusion model by Dayananda et al.[39,45] For this purpose, we analyzed the concentration profiles obtained by XRD in an earlier study[38] of halide diffusion in physically mixed $MAPbI_3$ and $MAPbBr_3$ powders at temperatures up to 90 °C. We extended the average interdiffusion model to derive the instantaneous diffusivity $D(t)$ that decays in a single-exponential fashion over time. The time dependence is a result of the disappearing concentration gradient that drives the interdiffusion.

We find a higher diffusion coefficient $D(t)$ for Br^- than for I^- for the complete halide exchange process at all investigated temperatures in the absence of IL. We attribute this mainly to the higher barrier for the formation of Br^- vacancies, which kinetically hinders the I^- diffusion into Br-rich phases. The addition of the IL $BMIMBF_4$ results in an overall accelerated diffusion process. The diffusion constants as well as activation energies for I^- and Br^- diffusion become nearly equal. We consider that this results from the $BMIM^+$ cation facilitating the formation of Br^- vacancies and shuttling halides between grains. In this way, the bottleneck of Br^- vacancies is removed so that the I^- diffusion is more expedited. The process is controlled by the thermal activation of the $BMIM^+$ cation. The concept of average effective interdiffusion coefficients may also be applied to, e.g., other additives and perovskites with different A-site cations, and thus allow for insights into their diffusivity. Hence, we provide a general model insofar that the model can be applied to any system where ion migration and associated concentration gradients can be tracked quantitatively. However, the data extraction, interpretation, and analysis need to be adjusted for the specific system considered.

Supporting Information

Supporting Information is available from the Wiley Online Library or from the author.

Acknowledgements

The author thanks Christopher Greve, Stavros Athanasopoulos, Maximilian Spies, Fatemeh Haddadi Barzoki, Simon Biberger, Werner Köhler, Philipp Ramming, Tianshan Xu, Andrei Stankevych, Maximilian Theis, and Meike Kuhn for fruitful discussions. The authors thank Ralf Moos for access to the planetary ball mill. H.G., A.K., and T.S. thank the DFG (Deutsche Forschungsgemeinschaft) for funding within project number 506 642 499 (SPP 2196/2). H. O. thanks the DFG for funding within project number 492 723 217 (CRC 1585 MultiTrans). P. P. thanks the DFG for funding within project number 464 648 186 (IRTG 2818 OPTEXC). The authors further thank Prof. Josef Breu for access to XRD machines.

Conflict of Interest

The authors declare no conflict of interest.

Data Availability Statement

The data that support the findings of this study are available from the corresponding author upon reasonable request.

Keywords

average effective interdiffusion coefficient, halide diffusion, halide ion exchange, ionic liquid, solid solution

Received: April 30, 2025
Revised: July 17, 2025
Published online: August 8, 2025

[1] Best Research-Cell Efficiency Chart.
[2] A. K. Jena, A. Kulkarni, T. Miyasaka, *Chem. Rev.* **2019**, *119*, 3036.
[3] G. Li, T. Zhang, N. Guo, F. Xu, X. Qian, Y. Zhao, *Angew. Chem., Int. Ed.* **2016**, *55*, 13460.
[4] C.-H. Kuan, H.-H. Shen, C.-F. Lin, *RSC Adv.* **2021**, *11*, 3264.
[5] M. Zhang, H. Yu, M. Lyu, Q. Wang, J.-H. Yun, L. Wang, *Chem. Commun.* **2014**, *50*, 11727.
[6] M. T. Hörantner, T. Leijtens, M. E. Ziffer, G. E. Eperon, M. G. Christoforo, M. D. McGehee, H. J. Snaith, *ACS Energy Lett.* **2017**, *2*, 2506.
[7] D. P. McMeekin, G. Sadoughi, W. Rehman, G. E. Eperon, M. Saliba, M. T. Hörantner, A. Haghighirad, N. Sakai, L. Korte, B. Rech, M. B. Johnston, L. M. Herz, H. J. Snaith, *Science* **2016**, *351*, 151.
[8] C. Yi, J. Luo, S. Meloni, A. Boziki, N. Ashari-Astani, C. Grätzel, S. M. Zakeeruddin, U. Röthlisberger, M. Grätzel, *Energy Environ. Sci.* **2016**, *9*, 656.
[9] A. M. A. Leguy, P. Azarhoosh, M. I. Alonso, M. Campoy-Quiles, O. J. Weber, J. Yao, D. Bryant, M. T. Weller, J. Nelson, A. Walsh, M. Schilfgaarde, P. R. F. Barnes, *Nanoscale* **2016**, *8*, 6317.
[10] T. Yokoyama, T.-B. Song, D. H. Cao, C. C. Stoumpos, S. Aramaki, M. G. Kanatzidis, *ACS Energy Lett.* **2017**, *2*, 22.
[11] E. T. Hoke, D. J. Slotcavage, E. R. Dohner, A. R. Bowring, H. I. Karunadasa, M. D. McGehee, *Chem. Sci.* **2015**, *6*, 613.
[12] M. U. Ali, H. Mo, A. U. Rehman, T. L. Leung, A. B. Djurišić, *Trends in Chemistry* **2024**, *6*, 248.
[13] A. J. Knight, A. D. Wright, J. B. Patel, D. P. McMeekin, H. J. Snaith, M. B. Johnston, L. M. Herz, *ACS Energy Lett.* **2019**, *4*, 75.
[14] T. Elmelund, B. Seger, M. Kuno, P. V. Kamat, *ACS Energy Lett.* **2020**, *5*, 56.
[15] S. Ruan, M.-A. Surmiak, Y. Ruan, D. P. McMeekin, H. Ebendorff-Heidepriem, Y.-B. Cheng, J. Lu, C. R. McNeill, *J. Mater. Chem. C* **2019**, *7*, 9326.
[16] E. M. Hutter, L. A. Muscarella, F. Wittmann, J. Versluis, L. McGovern, H. J. Bakker, Y.-W. Woo, Y.-K. Jung, A. Walsh, B. Ehrler, *Cell Reports Physical Science* **2020**, *1*, 100120.

[17] P. Nandi, C. Giri, D. Swain, U. Manju, S. D. Mahanti, D. Topwal, *ACS Appl. Energy Mater.* **2018**, *1*, 3807.
[18] Y. Daikoku, T. Yamada, A. Shimazaki, T. Nakamura, A. Wakamiya, Y. Kanemitsu, *J. Phys. Chem. Lett.* **2024**, *15*, 12341.
[19] X. Qi, S. Fang, Y. Miao, J. Wu, L. Yang, C. Yang, X. Wang, F. Zheng, F. Zhao, S. Shafique, Z. Hu, *Appl. Phys. Lett.* **2024**, *124*, 064103.
[20] I. L. Braly, R. J. Stoddard, A. Rajagopal, A. R. Uhl, J. K. Katahara, A. K.-Y. Jen, H. W. Hillhouse, *ACS Energy Lett.* **2017**, *2*, 1841.
[21] A. F. Gualdrón-Reyes, S. J. Yoon, E. M. Barea, S. Agouram, V. Muñoz-Sanjosé, Á. M. Meléndez, M. E. Niño-Gómez, I. Mora-Seró, *ACS Energy Lett.* **2019**, *4*, 54.
[22] Y. Zhao, P. Miao, J. Elia, H. Hu, X. Wang, T. Heumueller, Y. Hou, G. J. Matt, A. Osvet, Y.-T. Chen, M. Tarragó, D. de Ligny, T. Przybilla, P. Denninger, J. Will, J. Zhang, X. Tang, N. Li, C. He, A. Pan, A. J. Meixner, E. Spiecker, D. Zhang, C. J. Brabec, *Nat. Commun.* **2020**, *11*, 6328.
[23] A. J. Barker, A. Sadhanala, F. Deschler, M. Gandini, S. P. Senanayak, P. M. Pearce, E. Mosconi, A. J. Pearson, Y. Wu, A. R. Srimath Kandada, T. Leijtens, F. De Angelis, S. E. Dutton, A. Petrozza, R. H. Friend, *ACS Energy Lett.* **2017**, *2*, 1416.
[24] L. Tian, J. Xue, R. Wang, *Electronics* **2022**, *11*, 700.
[25] M. Kuno, M. C. Brennan, *Matter* **2020**, *2*, 21.
[26] M. C. Brennan, A. Ruth, P. V. Kamat, M. Kuno, *Trends in Chemistry* **2020**, *2*, 282.
[27] X. Zheng, S. Yang, J. Zhu, R. Liu, L. Li, M. Zeng, C. Lan, S. Li, J. Li, Y. Shi, C. Chen, R. Guo, Z. Zheng, J. Guo, X. Wu, T. Luan, Z. Wang, D. Zhao, Y. Rong, X. Li, *Energy Environ. Sci.* **2025**, *18*, 2995.
[28] J. Ma, L. Wang, K. He, Y. Sun, B. Li, Q. Zhao, B. Du, *J. Mater. Chem. C* **2024**, *12*, 10837.
[29] K. Zhang, X. Zhang, K. G. Brooks, B. Ding, S. Kinge, Y. Ding, S. Dai, M. K. Nazeeruddin, *Sol. RRL* **2023**, *7*, 2300115.
[30] G. L. Gutsev, A. I. Boldyrev, *Russ. Chem. Rev.* **1987**, *56*, 519.
[31] S. Bai, P. Da, C. Li, Z. Wang, Z. Yuan, F. Fu, M. Kawecki, X. Liu, N. Sakai, J. T.-W. Wang, S. Huettner, S. Buecheler, M. Fahlman, F. Gao, H. J. Snaith, *Nature* **2019**, *571*, 245.
[32] H. Kim, J. Lim, M. Sohail, M. K. Nazeeruddin, *Sol. RRL* **2022**, *6*, 2200013.
[33] H. D. B. Jenkins, K. P. Thakur, *J. Chem. Educ.* **1979**, *56*, 576.
[34] S. Katsuta, K. Imai, Y. Kudo, Y. Takeda, H. Seki, M. Nakakoshi, *J. Chem. Eng. Data* **2008**, *53*, 1528.
[35] M. Ue, *J. Electrochem. Soc.* **1994**, *141*, 3336.
[36] G. P. Nagabhushana, R. Shivaramaiah, A. Navrotsky, *Proc. Natl. Acad. Sci. USA* **2016**, *113*, 7717.
[37] P. Ramming, N. Leupold, K. Schötz, A. Köhler, R. Moos, H. Grüninger, F. Panzer, *J. Mater. Chem. C* **2021**, *9*, 11827.
[38] C. Greve, P. Ramming, M. Griesbach, N. Leupold, R. Moos, A. Köhler, E. M. Herzig, F. Panzer, H. Grüninger, *ACS Energy Lett.* **2023**, *8*, 5041.
[39] M. A. Dayananda, *Defect and Diffusion Forum* **1993**, *95–98*, 521.
[40] A. Laik, P. S. Gawde, K. Bhanumurthy, G. B. Kale, *Metall. Mater. Trans. A* **2008**, *39*, 733.
[41] A. Mehta, J. Dickson, R. Newell, D. D. Keiser, Y. Sohn, *J. Phase Equilib. Diffus.* **2019**, *40*, 482.
[42] S. Yang, S. Gao, W. Xue, B. Wu, D. Duan, *Surf. Coat. Technol.* **2023**, *473*, 130035.
[43] W. Liu, L. Long, Y. Ma, L. Wu, *J. Alloys Compd.* **2015**, *643*, 34.
[44] J. Priimets, Ü. Ugaste, *Defect and Diffusion Forum* **2012**, *326*, 209.
[45] S. Wollstadt, R. A. De Souza, O. Clemens, *J. Phys. Chem. C* **2021**, *125*, 2287.
[46] P. Sanchora, D. K. Pandey, D. Rana, A. Materny, D. K. Singh, *J. Phys. Chem. A* **2019**, *123*, 4948.
[47] H. Zai, Y. Ma, Q. Chen, H. Zhou, *J. Energy Chem.* **2021**, *63*, 528.
[48] X. Yan, W. Fan, F. Cheng, H. Sun, C. Xu, L. Wang, Z. Kang, Y. Zhang, *Nano Today* **2022**, *44*, 101503.
[49] F. H. Naqvi, J.-H. Ko, T. H. Kim, C. W. Ahn, Y. Hwang, *Curr. Appl. Phys.* **2022**, *44*, 150.
[50] W. Jiang, H. Di, H. Sun, C. Zhao, F. Liao, Y. Zhao, *J. Cryst. Growth* **2020**, *550*, 125880.
[51] R. M. Muslimawati, M. Manawan, A. Bahtiar, *J. Phys.: Conf. Ser.* **2022**, *2344*, 012002.
[52] C. C. Stoumpos, C. D. Malliakas, M. G. Kanatzidis, *Inorg. Chem.* **2013**, *52*, 9019.
[53] S. Bonomi, V. Armenise, G. Accorsi, S. Colella, A. Rizzo, F. Fracassi, L. Malavasi, A. Listorti, *Appl. Sci.* **2020**, *10*, 4775.
[54] A. Osherov, Y. Feldman, I. Kaplan-Ashiri, D. Cahen, G. Hodes, *Chem. Mater.* **2020**, *32*, 4223.
[55] M. Lai, A. Obliger, D. Lu, C. S. Kley, C. G. Bischak, Q. Kong, T. Lei, L. Dou, N. S. Ginsberg, D. T. Limmer, P. Yang, *Proc. Natl. Acad. Sci. U.S.A.* **2018**, *115*, 11929.
[56] T. Elmelund, R. A. Scheidt, B. Seger, P. V. Kamat, *ACS Energy Lett.* **2019**, *4*, 1961.
[57] M. Ghasemi, B. Guo, K. Darabi, T. Wang, K. Wang, C.-W. Huang, B. M. Lefler, L. Taussig, M. Chauhan, G. Baucom, T. Kim, E. D. Gomez, J. M. Atkin, S. Priya, A. Amassian, *Nat. Mater.* **2023**, *22*, 329.
[58] D. Pan, Y. Fu, J. Chen, K. J. Czech, J. C. Wright, S. Jin, *Nano Lett.* **2018**, *18*, 1807.
[59] A. Mannodi-Kanakkithodi, J.-S. Park, A. B. F. Martinson, M. K. Y. Chan, *J. Phys. Chem. C* **2020**, *124*, 16729.
[60] L. McGovern, M. H. Futscher, L. A. Muscarella, B. Ehrler, *J. Phys. Chem. Lett.* **2020**, *11*, 7127.
[61] Y. W. Woo, Y.-K. Jung, G. Y. Kim, S. Kim, A. Walsh, *Discov Mater* **2022**, *2*, 8.
[62] J. M. Azpiroz, E. Mosconi, J. Bisquert, F. D. Angelis, *Energy Environ. Sci.* **2015**, *8*, 2118.
[63] C. Lin, S. Li, W. Zhang, C. Shao, Z. Yang, *ACS Appl. Energy Mater.* **2018**, *1*, 1374.
[64] B. Zhang, Z. Hu, J. Su, Z. Gong, X. Guo, X. Chen, Y. Yang, Z. Lin, L. Ding, Y. Hao, J. Chang, *Angew. Chem.* **2025**, *64*, 202413550.
[65] S. G. Motti, D. Meggiolaro, S. Martani, R. Sorrentino, A. J. Barker, F. De Angelis, A. Petrozza, *Adv. Mater.* **2019**, *31*, 1901183.
[66] T. G. Kim, S. W. Seo, H. Kwon, J. Hahn, J. W. Kim, *Phys. Chem. Chem. Phys.* **2015**, *17*, 24342.
[67] W. M. Haynes, *Crc Handbook of Chemistry and Physics*, CRC Press LLC: Milton, UNITED KINGDOM **2016**.
[68] S. Maintz, V. L. Deringer, A. L. Tchougréeff, R. Dronskowski, *J. Comput. Chem.* **2016**, *37*, 1030.
[69] R. M. dos Santos, I. Ornelas–Cruz, A. C. Dias, M. P. Lima, J. L. F. Da Silva, *ACS Appl. Energy Mater.* **2023**, *6*, 5259.
[70] J. A. S. Laranjeira, S. A. Azevedo, F. A. La Porta, M. M. Ferrer, E. Longo, J. R. Sambrano, *J. Phys. Chem. C* **2024**, *128*, 11858.
[71] Y. Cao, T. Mu, *Ind. Eng. Chem. Res.* **2014**, *53*, 8651.
[72] B. A. Koscher, N. D. Bronstein, J. H. Olshansky, Y. Bekenstein, A. P. Alivisatos, *J. Am. Chem. Soc.* **2016**, *138*, 12065.
[73] Y.-R. Lee, Y.-T. Chung, T.-Y. Chiang, T. Hsieh, Y.-H. Su, J.-K. Wang, *ACS Omega* **2024**, *9*, 26439.
[74] K. Xu, S. P. Ding, T. R. Jow, Nonaqueous Electrolyte Development for Electrochemical Capacitors.